

Multibaric sampling for machine learning potential construction

Kazutoshi Miwa ^{*}*Toyota Central Research & Development Laboratories, Inc., Nagakute, Aichi 480-1192, Japan*

(Received 22 February 2021; accepted 21 April 2021; published 29 April 2021)

The on-the-fly machine learning potential (MLP) generation scheme is combined with the multibaric-isothermal (MUBA) ensemble simulation to construct the MLP applicable for the prediction of the phase stability under various pressures. The MUBA simulation performs a random walk in the volume space and provides an efficient way to sample physically relevant configurations over a wide range of volume. In the present MUBA formulation, the explicit construction of a bias potential to realize a random walk is not required. The sample structures for training are dynamically collected by the simulation using the MLP itself, in which the simultaneous error estimation is utilized to judge whether an updated structure should be added to the sample data set or not. The utility of the method is demonstrated for aluminum nitride. The MUBA ensemble is sampled using the hybrid Monte Carlo (HMC) method at 300 K. Starting from the metastable zinc-blende structure, the simulation correctly reproduces experimentally observed two phases, the wurtzite and rocksalt structures. During 600 000 configuration updates in the HMC sweeps, the total number of density-functional theory (DFT) calculations required is only 107. The constructed MLP shows high accuracy comparable to the DFT calculations.

DOI: [10.1103/PhysRevB.103.144106](https://doi.org/10.1103/PhysRevB.103.144106)

I. INTRODUCTION

Atomistic simulations such as molecular dynamics (MD) and Monte Carlo (MC) methods have successfully been applied in a wide variety of research fields [1,2]. In order to take desired statistics with isothermal and/or isobaric conditions as in experiments, various ensemble techniques were developed [3–10]. In these physical ensemble simulations, if the system falls into a local minimum on the potential energy surfaces surrounded by barriers much higher than its thermal energy, it is difficult to escape from this potential basin. To overcome this difficulty, the multithermal and multibaric algorithms were proposed [11–17], which are often referred to as the generalized ensembles. The multithermal ensemble is designed to realize a random walk in the potential energy space. This enables the simulation to sample the configurations efficiently in a wide range of temperatures without trapping in local minima. The isothermal ensemble averages at different temperatures can be obtained from a single simulation run by the reweighting technique [11]. Similarly, the multibaric simulation performs a random walk in the volume space and provides an efficient way to explore the configurations under various pressures. Pressure-induced structural phase transitions are commonly observed for solids. Nowadays, high-pressure techniques are a powerful tool to search for new materials with advanced functionalities [18–21]. Thus, the theoretical prediction of the phase stability as a function of pressure as well as temperature is an important issue in condensed matter physics.

The accuracy of the interatomic potentials is crucial in performing the atomistic simulations. First-principles

calculations based on density-functional theory (DFT) [22,23] allow us to describe the atomic interactions with an accurate quantum-mechanical treatment. Owing to high computational demands of DFT calculations, empirical interatomic potentials have also been used, particularly, in large-scale simulations. The reliability of these potentials, however, strongly depends on the potential functions and their parameters, which must be determined carefully. Since the structural phase transitions usually are accompanied by changes in coordination numbers and reconstruction of chemical bonds, it is often difficult to simulate them with the empirical potentials. An alternative approach to perform large-scale atomistic simulations is the machine learning potential (MLP) [24–27]. In the MLP, the atomic interactions are represented by a simple and flexible function. The function is chosen from a mathematical point of view rather than physical motivation and can treat different chemical environment and bonding on the same footing. Recently, the MLP approach was applied for the pressure-induced phase transition in gallium nitride [28].

We developed the automatic MLP generation scheme, self-learning and adaptive database (SLAD) [29]. In the SLAD, the sample structures for training are dynamically collected by MD simulations using the MLP itself, in which the simultaneous error estimation with the spilling factor [26] is utilized to judge whether an updated structure should be added to the sample data set or not. The expensive DFT calculations need to be performed only for the selected sample structures. This enables to improve the quality of the sample data set efficiently and systematically. Our MLP was successfully applied to various materials [26,29–32] and showed high computational efficiency with accuracy comparable to DFT calculations.

In this paper, the SLAD approach is combined with the multibaric ensemble simulation to generate MLP applicable

*miwa@cmp.tytlabs.co.jp

for the prediction of the phase stability under various pressures. To this end, the multibaric simulation is formulated so as to be free from the explicit construction of a bias potential that is usually required to realize a random walk in the volume space [15,17]. This feature is essential to apply the simulation to the on-the-fly MLP generation. The utility of the method is demonstrated for aluminum nitride (AlN), which has interesting and useful physical properties such as the wide band gap, high resistivity, high thermal conductivity, low thermal expansion coefficient, and large hardness. It is known that AlN crystallizes in the hexagonal wurtzite structure at ambient conditions and undergoes a structural phase transition to the cubic rocksalt structure at high pressure, 14–22 GPa [33–35].

The rest of this paper is organized as follows: Section II gives the formulation of the multibaric ensemble simulation and the MLP construction method. In Sec. III, the results of the multibaric simulations for AlN are presented, and the accuracy of the constructed MLP is examined. Section IV summarizes the main results of this study.

II. METHODOLOGY

A. Hybrid Monte Carlo method

The multibaric simulations are carried out using the hybrid Monte Carlo method (HMC) [36], which combines the advantages of the MD and MC simulations. It allows the global configuration updates and does not suffer from the discretization error due to a finite time-step size as MD algorithms do.

In this section, the isobaric-isothermal (NPT) ensemble sampling with the HMC method is considered. In the global configuration updates, the MD run with the barostat proposed by Wentzcovitch [9] is used to treat the variation of a cell shape. Introducing the scaling strain tensor ε , three lattice vectors $\{\mathbf{a}, \mathbf{b}, \mathbf{c}\}$ are represented by the reference ones $\{\mathbf{a}_0, \mathbf{b}_0, \mathbf{c}_0\}$ with the relation $\{\mathbf{a}, \mathbf{b}, \mathbf{c}\} = (1 + \varepsilon)\{\mathbf{a}_0, \mathbf{b}_0, \mathbf{c}_0\}$. The atom positions \mathbf{r}_i ($i = 1, \dots, N$) also are represented by the reduced coordinates \mathbf{r}'_i in the reference simulation box with the same scaling relation $\mathbf{r}_i = (1 + \varepsilon)\mathbf{r}'_i$. The Wentzcovitch's isobaric-isenthalpic (NPH) Hamiltonian is given by

$$\mathcal{H}_{NPH} = \sum_i \frac{\mathbf{p}'_i \cdot d^{-1} \mathbf{p}'_i}{2m_i} + U(\{(1 + \varepsilon)\mathbf{r}'_i\}) + PV + \frac{p_\varepsilon^2}{2W}. \quad (1)$$

Here, \mathbf{p}'_i are the momenta conjugate to \mathbf{r}'_i , m_i are the atom masses, $d = (1 + \varepsilon)^T(1 + \varepsilon)$, U represents the interatomic potential, V is the cell volume, and P is an external pressure. The fourth term is the fictitious kinetic energy for the barostat, which contains the fictitious mass W and momenta p_ε .

The flow of the NPT -HMC simulation is as follows: (i) For a given configuration, the scaling strain ε is set to zero ($\{\mathbf{a}_0, \mathbf{b}_0, \mathbf{c}_0\} = \{\mathbf{a}, \mathbf{b}, \mathbf{c}\}$, $\mathbf{r}'_i = \mathbf{r}_i$), and all the momenta including the fictitious ones of the barostat are refushed by the Maxwell distribution. (ii) The NPH -MD run is executed with a few time steps. (iii) Using the change in the Hamiltonian $\Delta\mathcal{H}_{NPH}$ due to the configuration update, the Metropolis criterion is applied to accept or reject the trial configuration. The acceptance probability is given by

$$p = \min[1, \exp(-\beta\Delta\mathcal{H}_{NPH})], \quad (2)$$

where $\beta (= \frac{1}{k_B T})$ is the inverse temperature. The second-order symplectic time integrator [37] is used in the MD run, which is the time reversible and the area preserving. These features guarantee to satisfy the detailed balance condition for the Markov process [36]. As seen in Eq. (2), it is not necessary to conserve the Hamiltonian strictly in the HMC simulation. This allows us to use a relatively large time-step size in the global MD updates.

B. Multibaric simulation

The NPT -HMC method mentioned in the previous section can be extended to the multibaric-isothermal (MUBA) simulation. In the MUBA simulation, the PV work term in the Hamiltonian of Eq. (1) is replaced by a bias potential δU ,

$$\mathcal{H}_{MUBA} = \sum_i \frac{\mathbf{p}'_i \cdot d^{-1} \mathbf{p}'_i}{2m_i} + U(\{(1 + \varepsilon)\mathbf{r}'_i\}) + \delta U(V) + \frac{p_\varepsilon^2}{2W}. \quad (3)$$

The condition for a random walk in the volume space is $\frac{\partial \mathcal{H}_{MUBA}}{\partial V} = 0$, from which the derivative of δU can be determined as

$$\frac{\partial \delta U}{\partial V} = \frac{N}{\beta V} - \frac{\partial U}{\partial V}. \quad (4)$$

Thus, the following procedure realizes the MUBA simulation. (i) The pressure is adjusted to $P = \frac{\partial \delta U}{\partial V}$ at the beginning of each HMC step. (ii) The trial configuration is generated by the NPH -MD update. (iii) The change in the Hamiltonian $\Delta\mathcal{H}_{MUBA}$ is used to judge whether the trial configuration is accepted or rejected with the Metropolis criterion. When the volume of the trial configuration is smaller (larger) than the predetermined value V_{\min} (V_{\max}), it is rejected to restrict the simulated volume range.

The generalized ensembles including the multibaric ensemble usually require the preliminary simulations to construct a bias potential before performing the production run [15,17]. When the on-the-fly MLP generation is combined with the conventional generalized ensemble approach, the bias potential has to be constructed with DFT calculations, which is very time consuming. The advantage of the present method is that the bias potential does not need to be constructed explicitly. The random walk is realized by the derivative of δU [Eq. (4)] that is able to be calculated analytically.

As shown in Sec. III, the MUBA simulation requires a relatively large number of HMC steps to explore an entire volume range of interest. To enforce the search away from visited volumes, a history-dependent histogram potential [13,38] is additionally introduced to the Hamiltonian of Eq. (3),

$$\Delta\delta U(V) = \Delta\delta U_0(V) + k_B T \ln h(V), \quad (5)$$

where $h(V)$ is the histogram with a finite bin size. The initial conditions are $\Delta\delta U_0(V) = 0$ and $h(V) = 1$. The histogram is updated at each HMC step. The derivative of this histogram potential $\frac{\partial \Delta\delta U}{\partial V}$ to be added to Eq. (4) is evaluated numerically using the cubic splines interpolation. When the highest value of $h(V)$ exceeds the criterion $h_{\max} = 1000$, the histogram potential is reset to be $\Delta\delta U_0(V) = \Delta\delta U(V)$ and $h(V) = 1$.

Although the bias potential is not explicitly constructed in our algorithm, it can be done after the simulation so that

one can calculate the the NPT ensemble averages from the MUBA simulation by using the reweighting technique [11] as in the conventional generalized ensemble methods. This point is briefly described below, though this technique is unnecessary for the MLP training. After the well-converged MUBA simulation is completed, the bias potential can be constructed from the following relation with an irrelevant constant,

$$\delta U(V) = \int_{V_0}^V \langle P(v) \rangle dv = \frac{N}{\beta} \ln \left(\frac{V}{V_0} \right) + \langle U(V_0) \rangle - \langle U(V) \rangle, \quad (6)$$

where V_0 is an arbitrary reference volume and $\langle \dots \rangle$ means the MUBA ensemble average.

C. Machine learning potential

The formulation of our MLP is briefly summarized. For simplicity, a monoatomic system is explained here. The details of our formulation including the extension to a multiatomic species system can be found in Ref. [26]. Our descriptor \mathbf{g} to characterize local atomic geometries is the power spectrum of the Fourier coefficients in the spherical coordinates. The geometry around the l th atom located at \mathbf{r}_l is represented by

$$\mathbf{g}^l = \mathbf{g}_{nl}^l = \sum_{m=-l}^l f_{nlm}^l f_{nlm}^l, \quad (7)$$

with

$$f_{nlm}^l = \sum_{i \neq l} f_{\text{cut}}(r_i^l) j_l(q_n r_i^l) Y_{lm}(\hat{\mathbf{r}}_i^l), \quad (8)$$

where $\mathbf{r}_i^l = \mathbf{r}_i - \mathbf{r}_l$, $r_i^l = |\mathbf{r}_i^l|$, j_l are the spherical Bessel functions, Y_{lm} are the real spherical harmonics, and f_{cut} is a smooth radial cutoff function with compact support. The sampling wave-vector lengths are set to be $q_n = 2\pi n/r_{\text{cut}}$, where r_{cut} is a cutoff radius of f_{cut} . The similarity measure between two local geometries is given by

$$d^2(\mathbf{g}^l, \mathbf{g}^j) = \sum_{n=0}^{n_{\text{max}}} \sum_{l=0}^{l_{\text{max}}} |g_{nl}^l - g_{nl}^j|^2, \quad (9)$$

where n_{max} and l_{max} control the resolution of the descriptors. Using the similarity measures, the energy U is represented by a sum of weighted Gaussians:

$$U = \sum_{J \in \text{ref}} \alpha_J \sum_I \mathcal{Q}(\mathbf{g}^l, \mathbf{g}^j), \quad (10)$$

where $\mathcal{Q}(\mathbf{g}^l, \mathbf{g}^j) = \exp[-d^2(\mathbf{g}^l, \mathbf{g}^j)/(2\theta^2)]$, α are the regression coefficients, θ are the scale parameter, and J runs over the reference descriptors. The reference descriptors are generated from the local configurations in the sample data set by the recursive bisection method with the k -means clustering, which removes highly correlated configurations and thus enhances the computational efficiency without significant loss of accuracy. The spilling factor for the simultaneous error estimation is defined as

$$s(\mathbf{g}) = 1 - \sum_{I \in \text{ref}} \sum_{J \in \text{ref}} \mathcal{Q}(\mathbf{g}, \mathbf{g}^j) \mathcal{Q}^{-1}(\mathbf{g}^l, \mathbf{g}^j) \mathcal{Q}(\mathbf{g}^l, \mathbf{g}), \quad (11)$$

TABLE I. Parameters for MLP construction. The scale parameter θ , regularization parameter λ , descriptor expansion parameters, n_{max} and l_{max} , cutoff radius r_{cut} , normalization parameters \mathcal{D}^{-1} , spilling factor tolerance s_{large} , and recursive bisection criterion δr^2 .

MLP parameters	
θ	0.5
λ	1×10^{-3}
n_{max}	12
l_{max}	6
r_{cut} (bohr)	8
$\mathcal{D}_{\text{energy}}^{-1}$ (hartree/atom)	1×10^{-4}
$\mathcal{D}_{\text{force}}^{-1}$ (hartree/bohr)	1×10^{-3}
$\mathcal{D}_{\text{stress}}^{-1}$ (GPa)	0.1
s_{large}	0.02
δr^2	0.01

which is zero when the geometry \mathbf{g} is fully projected by the reference descriptors, whereas $s = 1$ when \mathbf{g} has no overlaps between them. The analytic evaluation of the atomic force \mathbf{F}_l and stress σ is straightforward.

For a given sample data set, the regression coefficients are determined by minimizing the squared sum of residuals with the standard L_2 regularization. To enhance the accuracy of the MLP, in addition to the residuals of the energy, those of the atomic force and stress also are utilized. The normalization parameters \mathcal{D} for the energy, force, and stress are introduced to make them dimensionless and treat the quantities with different physical units on the same footing, namely, $X \rightarrow \mathcal{D}_X X$ ($X = E, \mathbf{F}_l, \sigma$).

The MLP construction is carried out with the following SLAD procedure: (i) During the HMC simulations with the MLP, a sample structure is collected when the maximum value of the spilling factors exceeds the tolerance $s_{\text{large}} = 0.02$ or 2000 HMC steps proceed without any sample collection. Once a sample structure is collected, the HMC simulation is suspended. (ii) The DFT calculation is performed for a new sample structure, and the result is added to the sample data set. (iii) The MLP is reconstructed with the updated sample data set. (iv) The HMC simulation is restarted from the latest accepted configuration. The parameters for the MLP construction are summarized in Table I.

The DFT calculations for the collected sample structures are performed using the ultrasoft pseudopotential method [39–42]. The cutoff energies are 15 and 96 hartrees for the wave function and charge density, respectively, and a $2 \times 2 \times 2$ k -point mesh is used for the Brillouin zone integration. The generalized gradient approximation proposed by Perdew, Burke, and Ernzerhof (GGA-PBE) [43] is adopted for the exchange-correlation energy.

III. RESULTS AND DISCUSSION

The MUBA simulation is applied for AlN. The calculations are performed for the supercell containing 32 formula units (64 atoms) at temperature $T = 300$ K. The volume range is restricted to be $V = 448\text{--}768 \text{ \AA}^3$ and the simulation period is taken to be 200 000 HMC steps. Since the thermodynamic averages for classical systems do not depend on the atomic

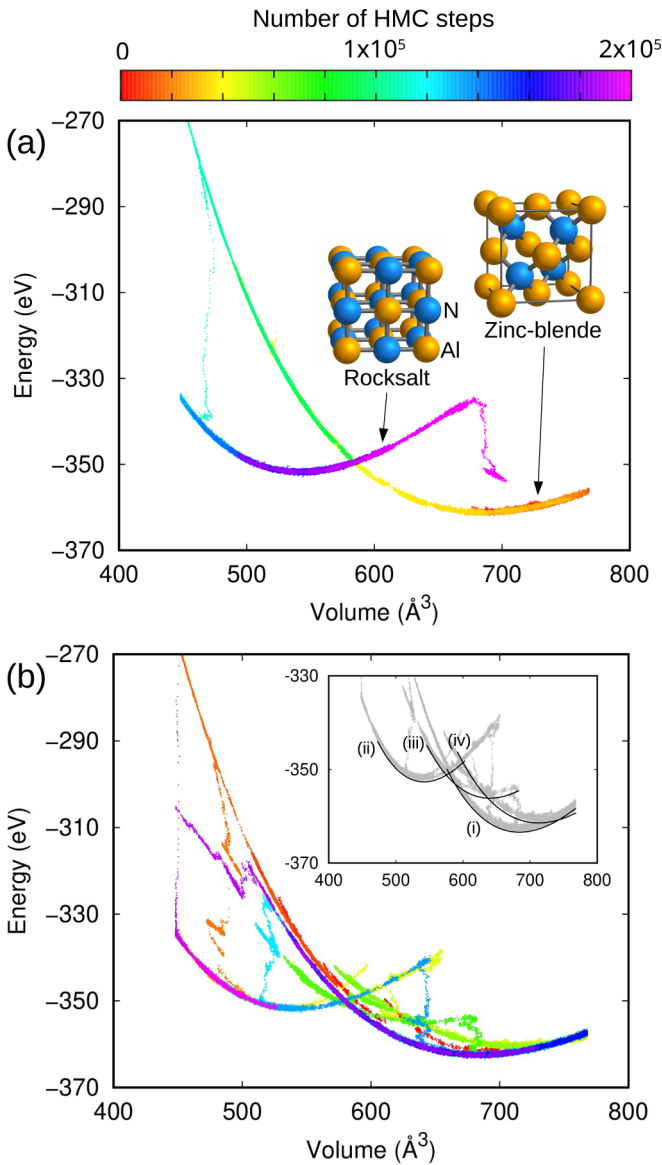


FIG. 1. Energy-volume relations for AlN obtained by the MUBA simulations (a) without and (b) with the histogram potential. Colors represent the number of HMC steps. In the inset of (b), the MUBA sampling points after 40 000 HMC step are compared with the EOSs calculated by DFT for four phases, (i) wurtzite, (ii) rocksalt, (iii) hexagonal, and (iv) tetragonal phases. The energies of the EOSs are shifted by $Nk_B T = 1.7$ eV.

masses, those of Al and N are set to be unity in the MUBA simulation for simplicity. Three MD steps with the time-step size of 0.97 fs are used for the configuration updates. The simulation is started from the metastable zinc-blende structure. The lattice constant is set to the theoretical value and the atom positions are randomly displaced. The initial MLP is constructed for this randomized structure.

Figure 1(a) depicts the energy-volume relation obtained by the MUBA simulation without the histogram potential. The simulation samples a whole volume range and the transition to the rocksalt structure can be observed. However, the sampling is not sufficient, in particular for a large volume region. In fact, the most stable wurtzite phase does not appear in this profile.

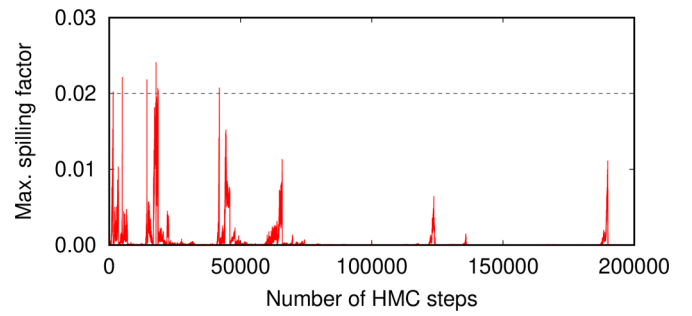


FIG. 2. Profile of the maximum spilling factor during the MUBA simulation with the histogram potential. A dashed (gray) line represents the spilling factor tolerance $s_{\text{large}} = 0.02$.

More HMC sweeps are necessary to explore a entire volume range sufficiently.

The MUBA simulation is repeated with the histogram potential, where the volume range is discretized by 30 bins. The result is given in Fig. 1(b). As can be seen, the histogram potential enhances a random walk in the volume space. Figure 2 shows the profile of the maximum spilling factor. Though several spikes exceed the tolerance s_{large} during the first 50 000 HMC steps, they are quickly attenuated due to the dynamical data collection with the SLAD. In the remaining steps, the factors are always kept smaller than the tolerance. Thus, high accuracy is expected for the present MUBA simulation with the on-the-fly MLP generation. The accuracy of the constructed MLP will be discussed later.

First, the result of the MUBA simulation with the histogram potential is discussed. In this profile, four concave curves are found as shown in the inset of Fig. 1(b). Here, the solid lines show the Murnaghan's equation of state (EOS) [44] fitted to the DFT total energies and are rigidly shifted by $Nk_B T = 1.7$ eV for better comparison. The lines labeled by (i) and (ii) are the results for the wurtzite and rocksalt structures, respectively. The agreement between the MUBA sampling points and these EOSs is quite good. To check the crystal structures in the MUBA simulation for both lines, the average structures are calculated from the sampling points located around the local minima [177 000 – 180 000 and 130 000 – 133 000 HMC steps for the lines (i) and (ii), respectively], and their x-ray diffraction (XRD) patterns are simulated using the superposition of atomic densities. In Fig. 3, the simulated XRD patterns are compared with the references calculated for the DFT-optimized structures (see Table II). It can be confirmed that the MUBA simulation correctly reproduces experimentally observed two structures, the wurtzite and rocksalt structures. Additional two phases labeled by (iii) and (iv) are the hexagonal structure with the symmetry of $P6_3/mmc$ and the tetragonal structure with $P4_2/mnm$, respectively (see Table II and the insets of Fig. 5). To our knowledge, these two structures have not yet been reported. For both structures, the agreement between the MUBA sampling points and the EOSs is reasonably good.

The number of the sample structures collected in the MUBA simulation, for which the DFT calculations were performed, is 107. This is only 0.02% of the total number of the configuration updates. The simulation is considerably accelerated by the dynamical data collection with the SLAD.

TABLE II. Results of structural optimization using MLP and DFT. Lattice constants a and c (Å), atom positions in Wyckoff notation, and cohesive energy E_{coh} (eV/atom).

Structure		a	c	Atom positions	E_{coh}
Wurtzite	MLP	3.133	5.027	Al($2b$ $z = 0$), N($2b$ $z = 0.3812$)	5.70
$P6_3mc$	DFT	3.133	5.028	Al($2b$ $z = 0$), N($2b$ $z = 0.3811$)	5.70
Rocksalt	MLP	4.073		Al($4a$), N($4b$)	5.54
$Fm\bar{3}m$	DFT	4.076		Al($4a$), N($4b$)	5.54
Zinc-blende	MLP	4.409		Al($4a$), N($4c$)	5.68
$F\bar{4}3m$	DFT	4.409		Al($4b$), N($4c$)	5.68
Hexagonal	MLP	3.314	4.212	Al($2c$), N($2d$)	5.59
$P6_3/mmc$	DFT	3.318	4.194	Al($2c$), N($2d$)	5.59
Tetragonal	MLP	5.337	3.127	Al($4f$ $x = 0.8230$), N($4g$ $x = 0.8156$)	5.67
$P4_2/mnm$	DFT	5.339	3.124	Al($4f$ $x = 0.8231$), N($4g$ $x = 0.8156$)	5.67

Next, the accuracy of the constructed MLP is considered. The scatter plots for the total energy, force, and macroscopic stress are shown in Fig 4, where 40 test configurations are selected from the MUBA simulation every 5000 HMC steps. The MLP reproduces the DFT results very well. The mean absolute errors for the test (training) data set

are 4.6×10^{-5} (2.5×10^{-5}) hartree/atom, 1.5×10^{-3} (1.5×10^{-3}) hartree/bohr, and 0.27 (0.05) GPa for the total energy, force, and macroscopic stress, respectively. The difference between the prediction errors for the training and test data sets is small, suggesting that the physically relevant configuration space is suitably covered with the sample structures in the training data set. In Table II, the structural parameters optimized by the MLP for four phases found in the MUBA simulation as well as the zinc-blende structure are compared with the DFT ones. The agreement between them is very good.

Figure 5 depicts the relative enthalpy changes as a function of pressure. Very good agreement between the results of the MLP and DFT calculations is found for this relation, too. The coordination number is four in the wurtzite, zinc-blende, and tetragonal structures, five in the hexagonal structure, and six in the rocksalt structure. The MLP generated with the MUBA sampling possesses high accuracy and flexibility to describe the different chemical environment under various pressures. In Fig. 5, it is found that the wurtzite structure is the most stable phase at ambient pressure and the rocksalt phase becomes more stable under high pressures, as widely reported in literature. The transition pressure from the wurtzite to rocksalt structure is evaluated to be 13 GPa which agrees reasonably with the experimental data of 14 – 22 GPa [33–35]. The calculated volume reduction associated with the transition is 20%, which also is in good agreement with the experimental values of 18 – 19% [33,34]. The enthalpy of the zinc-blende phase is slightly higher than that of the wurtzite phase by about 20 meV/atom regardless of pressures. Because there are no positive pressure regions where the hexagonal or tetragonal phase becomes thermodynamically most stable [45], it will be difficult to observe both phases in the experiments.

The Γ -phonon frequencies are calculated for the wurtzite and rocksalt structures using the constructed MLP with the frozen phonon approach. The finite atomic displacements are taken to be ± 0.01 Å. The linear-response phonon calculations based on DFT [40,46] are also carried out for comparison. To check the applicability of the MLP to volume changes, the calculations are performed under three different pressures, $P = 0, 15,$ and 30 GPa, where the structures are optimized by each method. Since AlN is a polar crystal, the infrared active modes are divided into the transverse optical (TO) and longitudinal optical (LO) modes. The LO modes involve

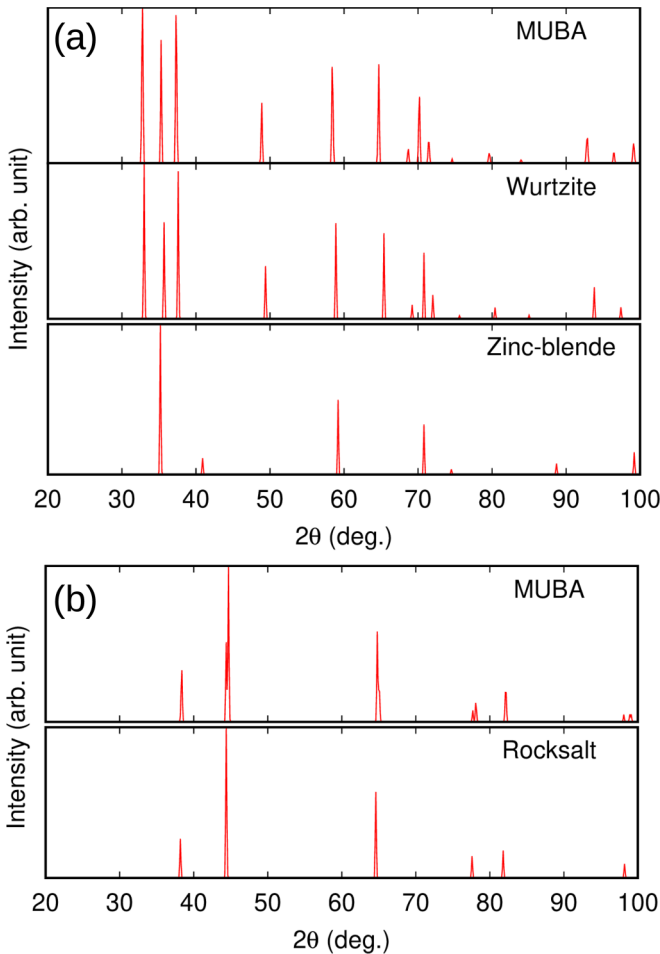


FIG. 3. Simulated XRD patterns for the average structures around the local minima of the lines (i) and (ii) in the inset of Fig 1(b). The references of the wurtzite, zinc-blende, and rocksalt structures are calculated for the DFT-optimized structures given in Table II.

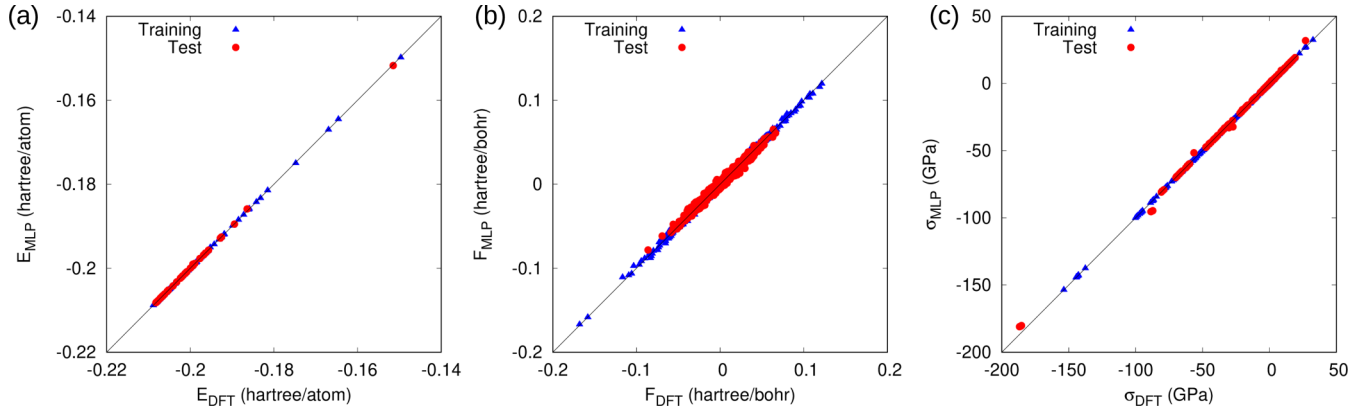


FIG. 4. Scatter plots for (a) total energy, (b) force, and (c) macroscopic stress.

contributions of the macroscopic electric field induced by lattice dynamics and cannot be described by classical force-field methods. Thus, the TO mode frequencies only are considered for the infrared active modes here. The calculated Γ -phonon frequencies are summarized in Table III. The frequencies calculated by the MLP are in good agreement with the DFT results, whose errors are within a few meV. Increasing the pressure from 0 to 30 GPa, the most modes exhibit upward frequency shifts by more than 10 meV. An exception is the lowest-lying E_2 mode in the wurtzite structure, which is kept almost constant. The second lowest-lying B_1 mode also shows a small upward shift less than 10 meV. The MLP correctly describes the pressure dependence of each phonon mode.

Table IV shows pressure dependence of the elastic constants of the wurtzite and rocksalt structures. The values calculated by the MLP agree reasonably with the DFT results. The mean absolute error is 9 GPa. Both phases become harder as the pressure rises. The experimental value for the

zero-pressure bulk modulus of wurtzite AlN was reported to be 208 GPa [33]. The calculations (both MLP and DFT) underestimate the bulk modulus by 9% because of the under-binding nature of GGA-PBE.

Finally, the coefficient of thermal expansion is predicted for the wurtzite phase using the isobaric-isothermal MD simulation with the MLP. The supercell containing 1024 atoms is used. The temperature range is taken to be $T = 150\text{--}300$ K with an interval of 50 K and the target pressure is fixed at $P = 0$ GPa. After 10 000 MD steps for equilibration, 50 000 MD steps are carried out to take the statistics. A good linear relationship is found between the volume and temperature, from the slope of which the thermal expansion coefficient is predicted to be $6.6 \times 10^{-6} \text{ K}^{-1}$. The agreement with the experimental value ($4.4 \times 10^{-6} \text{ K}^{-1}$ [47]) is relatively good. The overestimation of the coefficient most likely is related with the underestimation of the bulk modulus.

IV. SUMMARY

In this paper, the automatic MLP generation scheme, SLAD, has been combined with the multibaric-isothermal ensemble simulation. The MUBA simulation performs a random walk in the volume space and provides an efficient way to sample the physically relevant configurations over a wide range of volume. During the simulation, the sample structures for training are dynamically collected with the aid of the spilling factor, which enable to improve the quality of the

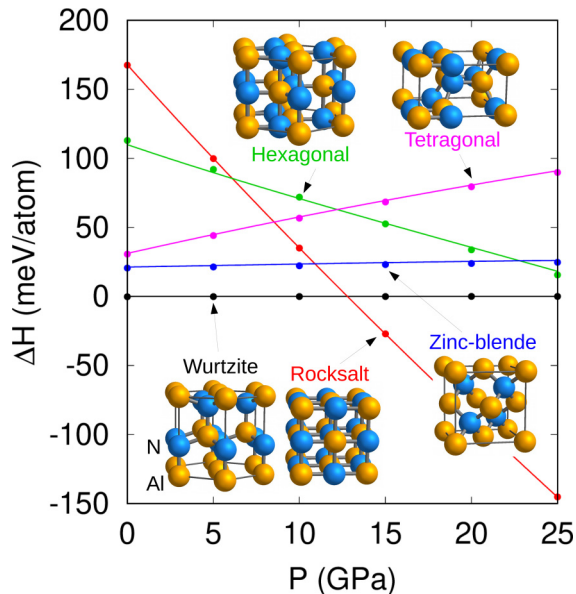


FIG. 5. Relative enthalpy changes ΔH as a function of pressure P . The enthalpy of the wurtzite phase calculated by the MLP is chosen as the reference. The solid lines and filled circles represent the MLP and DFT results, respectively.

TABLE III. Optical Γ -phonon frequencies (meV) under three different pressures P (GPa). TO mode frequencies only are given for the infrared active modes.

Structure	Mode	$P = 0$		$P = 15$		$P = 30$	
		MLP	DFT	MLP	DFT	MLP	DFT
Wurtzite	E_2	29	29	29	29	28	29
	B_1	65	66	69	70	71	74
	A_1	74	74	81	81	87	87
	E_2	78	79	87	88	95	96
	E_1	81	80	89	89	94	96
	B_1	87	87	95	94	99	101
Rocksalt	T_{1u}	55	55	64	63	66	70

TABLE IV. Bulk modulus B (GPa) and elastic stiffness constants $C_{\alpha\beta}$ (GPa) under three different pressures P (GPa). For hexagonal wurtzite, $C_{66} = (C_{11} - C_{12})/2$.

Structure		$P = 0$		$P = 15$		$P = 30$	
		MLP	DFT	MLP	DFT	MLP	DFT
Wurtzite	B	190	192	253	248	292	300
	C_{11}	388	397	467	462	498	515
	C_{12}	113	115	183	177	229	240
	C_{13}	83	84	140	138	197	198
	C_{33}	379	373	431	422	420	434
	C_{44}	118	118	131	125	129	129
	C_{66}	137	141	142	142	135	137
Rocksalt	B	246	250	323	309	352	364
	C_{11}	381	421	539	544	631	662
	C_{12}	180	166	215	193	213	215
	C_{44}	299	303	319	327	329	347

sample data set efficiently and systematically. In our MUBA formulation, the explicit construction of a bias potential to realize a random walk is not required. This feature is essen-

tial to apply the MUBA simulation to the on-the-fly MLP generation.

The utility of the method has been demonstrated for AlN. The MUBA ensemble is sampled using the HMC method at 300 K. Starting from the metastable zinc-blende structure, experimentally observed two phases, the wurtzite and rocksalt structures, are correctly sampled in the MUBA simulation. During 600 000 configuration updates in the HMC sweeps, the total number of the DFT calculations required is only 107. The constructed MLP possesses high accuracy comparable to the DFT calculations and can be applied to a variety of the crystal structures with the different chemical environment under various pressures. Note that the detection of the wurtzite-to-rocksalt transition in this paper is purely theoretical prediction, since the structural information used to execute the MUBA simulation is only that of metastable zinc-blende AlN.

ACKNOWLEDGMENTS

I thank R. Jinnouchi, J Lee, K. Sato, R. Asahi and T. Kimura for useful discussions.

- [1] M. E. Tuckerman and G. J. Martyna, *J. Phys. Chem. B* **104**, 159 (2000).
- [2] D. P. Landau and K. Binder, *A Guide to Monte Carlo Simulations in Statistical Physics*, 4th ed. (Cambridge University Press, Cambridge, 2014).
- [3] N. Metropolis, A. W. Rosenbluth, M. N. Rosenbluth, A. H. Teller, and E. Teller, *J. Chem. Phys.* **21**, 1087 (1953).
- [4] I. McDonald, *Mol. Phys.* **23**, 41 (1972).
- [5] H. C. Andersen, *J. Chem. Phys.* **72**, 2384 (1980).
- [6] M. Parrinello and A. Rahman, *Phys. Rev. Lett.* **45**, 1196 (1980).
- [7] S. Nosé, *Mol. Phys.* **52**, 255 (1984).
- [8] W. G. Hoover, *Phys. Rev. A* **31**, 1695 (1985).
- [9] R. M. Wentzcovitch, *Phys. Rev. B* **44**, 2358 (1991).
- [10] S. Nosé, *J. Phys. Soc. Jpn.* **70**, 75 (2001).
- [11] A. M. Ferrenberg and R. H. Swendsen, *Phys. Rev. Lett.* **61**, 2635 (1988).
- [12] B. A. Berg and T. Neuhaus, *Phys. Rev. Lett.* **68**, 9 (1992).
- [13] F. Wang and D. P. Landau, *Phys. Rev. Lett.* **86**, 2050 (2001).
- [14] M. S. Shell, P. G. Debenedetti, and A. Z. Panagiotopoulos, *Phys. Rev. E* **66**, 056703 (2002).
- [15] H. Okumura and Y. Okamoto, *Phys. Rev. E* **70**, 026702 (2004).
- [16] H. Okumura, *J. Phys. Soc. Jpn.* **81**, SA001 (2012).
- [17] P. M. Piaggi and M. Parrinello, *Phys. Rev. Lett.* **122**, 050601 (2019).
- [18] J. P. S. Walsh and D. E. Freedman, *Acc. Chem. Res.* **51**, 1315 (2018).
- [19] V. L. Solozhenko and E. Gregoryanz, *Mater. Today* **8**, 44 (2005).
- [20] A. P. Drozdov, M. I. Erements, I. A. Trojan, V. Ksenofontov, and S. I. Shylin, *Nature (London)* **525**, 73 (2015).
- [21] E. Snider, N. Dasenbrock-Gammon, R. McBride, M. Debessai, H. Vindana, K. Vencatasamy, K. V. Lawler, A. Salamat, and R. P. Dias, *Nature (London)* **586**, 373 (2020).
- [22] P. Hohenberg and W. Kohn, *Phys. Rev.* **136**, B864 (1964).
- [23] W. Kohn and L. J. Sham, *Phys. Rev.* **140**, A1133 (1965).
- [24] J. Behler and M. Parrinello, *Phys. Rev. Lett.* **98**, 146401 (2007).
- [25] A. P. Bartók, M. C. Payne, R. Kondor, and G. Csányi, *Phys. Rev. Lett.* **104**, 136403 (2010).
- [26] K. Miwa and H. Ohno, *Phys. Rev. B* **94**, 184109 (2016).
- [27] R. Jinnouchi, K. Miwa, F. Karsai, G. Kresse, and R. Asahi, *J. Phys. Chem. Lett.* **11**, 6946 (2020).
- [28] Q. Tong, X. Luo, A. A. Adeleke, P. Gao, Y. Xie, H. Liu, Q. Li, Y. Wang, J. Lv, Y. Yao, and Y. Ma, *Phys. Rev. B* **103**, 054107 (2021).
- [29] K. Miwa and H. Ohno, *Phys. Rev. Materials* **1**, 053801 (2017).
- [30] K. Miwa and R. Asahi, *Phys. Rev. Materials* **2**, 105404 (2018).
- [31] K. Miwa and R. Asahi, *Int. J. Hydrogen Energy* **44**, 23708 (2019).
- [32] K. Miwa and R. Asahi, *Solid State Ionics* **361**, 115567 (2021).
- [33] M. Ueno, A. Onodera, O. Shimomura, and K. Takemura, *Phys. Rev. B* **45**, 10123 (1992).
- [34] Q. Xia, H. Xia, and A. L. Ruoff, *J. Appl. Phys.* **73**, 8198 (1993).
- [35] S. Uehara, A. O. T. Masamoto, M. Ueno, O. Shimomura, and K. Takemura, *Phys. Chem. Solids* **58**, 2093 (1997).
- [36] B. Mehlig, D. W. Heermann, and B. M. Forrest, *Phys. Rev. B* **45**, 679 (1992).
- [37] H. Yoshida, *Phys. Lett. A* **150**, 262 (1990).
- [38] U. H. E. Hansmann and L. T. Wille, *Phys. Rev. Lett.* **88**, 068105 (2002).
- [39] D. Vanderbilt, *Phys. Rev. B* **41**, 7892 (1990).
- [40] K. Miwa, *Phys. Rev. B* **84**, 094304 (2011).
- [41] K. Miwa, *Phys. Rev. B* **97**, 075143 (2018).
- [42] K. Miwa and R. Asahi, *Phys. Rev. B* **102**, 174313 (2020).
- [43] J. P. Perdew, K. Burke, and M. Ernzerhof, *Phys. Rev. Lett.* **77**, 3865 (1996).
- [44] F. D. Murnaghan, *Proc. Natl. Acad. Sci. USA* **30**, 244 (1944).
- [45] The tetragonal structure is found to be the most stable phase below -10 GPa.
- [46] S. Baroni, S. de Gironcoli, A. Dal Corso, and P. Giannozzi, *Rev. Mod. Phys.* **73**, 515 (2001).
- [47] X. Ma, Y. F. Zhao, W. J. Tian, Z. Qian, H. W. Chen, Y. Y. Wu, and X. F. Liu, *Sci. Rep.* **6**, 34919 (2016).